ACS APPLIED NANO MATERIALS

www.acsanm.org Article

# Luminescent Silicon Nanosheet Paracrystals from Elemental- and Hydride-Based Syntheses of $CaSi_2$ Precursors: Implications for Photonic and Optoelectronic Applications

Bradley J. Ryan, Gourab Bhaskar, Jeremy B. Essner, Abhijit Bera, Rick W. Dorn, Yuqi Guo, Qing Hua Wang, Aaron J. Rossini, Julia V. Zaikina, Luke T. Roling, and Matthew G. Panthani*

Cite This: *ACS Appl. Nano Mater.* 2023, 6, 10054−10063 Read Online

ACCESS | Metrics & More | Article Recommendations | Supporting Information



**ABSTRACT:** Layered silicon nanosheets (SiNSs) have attracted considerable attention owing to their unique combination of chemical and physical properties, which makes them an exciting candidate for next-generation on-chip light sources and lasers. Despite over 150 years of research on SiNSs, the effects of the $CaSi_2$ precursor quality on SiNSs have not been studied. Here, we report a comparison of $CaSi_2$ (and SiNSs derived therefrom) synthesized from two reaction pathways: (1) melting Ca and Si (elemental melting, or EM-$CaSi_2$) and (2) the less-explored reaction between $CaH_2$ and Si (hydride synthesis, or HS-$CaSi_2$). We demonstrate that both reaction pathways lead to $CaSi_2$, but the HS-$CaSi_2$ pathway requires only a single step without the need to melt the $CaSi_2$ product and at a temperature below the peritectic decomposition of $CaSi_2$. We find that the EM-$CaSi_2$ exhibits grains that lay flat against the substrate, whereas the HS-$CaSi_2$ has little preferred orientation. We deintercalated both EM- and HS-$CaSi_2$ with HCl at −35 °C to yield hydrogen-terminated SiNSs. We characterized the SiNSs and found that the HS-SiNSs and EM-SiNSs exhibit properties that are nearly identical, with the exception that the morphology of the precursor is imparted to the SiNSs. These results provide the community with a one-step method to synthesize $CaSi_2$ and demonstrate that the morphology of $CaSi_2$ and SiNSs can be controlled with different synthetic techniques.

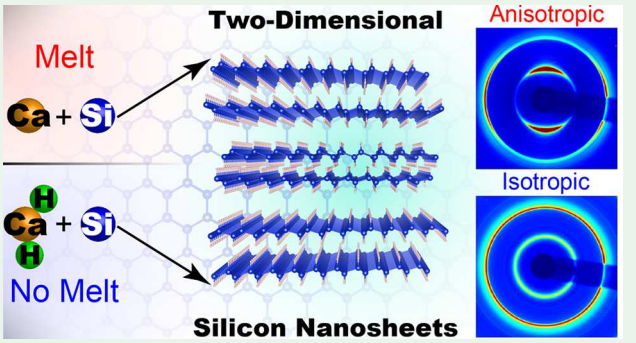


**KEYWORDS:** *optoelectronic, silicon nanosheets, photoluminescence, spectroscopy, preferred orientation*

## INTRODUCTION

Atomically thin, layered silicon nanosheets (SiNSs), sometimes referred to as layered polysilane,[1] have attracted attention for their applications as next-generation semiconductors,[2−6] catalysts,[7−9] and high-capacity anodes for energy-storage devices.[10−15] Furthermore, their luminescence and electronic transport properties have also been of particular interest due to their potential as a two-dimensional (2D) light-emitting semiconductor that is compatible with the existing complementary metal-oxide-semiconductor (CMOS) infrastructure.[16] Such CMOS-compatible, light-emitting semiconductors that seamlessly merge microelectronics with optical functionality are relevant to next-generation computing technologies,[38] such as integrated photonics.[17,18] Hydrogen-terminated SiNSs are typically synthesized by topotactic deintercalation of calcium disilicide ($CaSi_2$) with aqueous hydrochloric acid (HCl).[19] $CaSi_2$ is a layered Zintl phase consisting of anionic, buckled-honeycomb silicon (Si) monolayers intercalated with calcium (Ca) cations.[20] Given the potential of SiNSs for optoelectronics and computing applications, the importance of high-quality $CaSi_2$ precursors becomes much more apparent, as impurities in semiconductors can lead to undesirable properties.

SiNSs are frequently synthesized from a commercially available $CaSi_2$ precursor.[8,13,21] However, commercially available $CaSi_2$ sources are often of "technical grade", meaning they do not have any established purity regulations; "technical grade" chemicals are considered the least pure grade. Often, industrial and military production of $CaSi_2$ utilizes the carbothermic reduction process wherein quartzite is combined with carbon and calcium oxide or calcium carbonate to yield $CaSi_2$ and carbon monoxide;[22,23] these precursors often contain impurities. Unsurprisingly, commercial sources of $CaSi_2$ have also been reported to contain large quantities of impurities, including bulk silicon and iron silicides, which then

**Received:** January 17, 2023
**Accepted:** March 14, 2023
**Published:** June 8, 2023

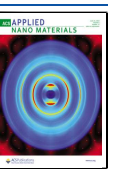




https://doi.org/10.1021/acsanm.3c00001
*ACS Appl. Nano Mater.* 2023, 6, 10054−10063

contaminate the synthesized SiNSs.[21,24] Such contamination poses a challenge when identifying structure−property relationships for SiNSs derived from these $CaSi_2$ sources. Thus, it is crucial to synthesize high-purity $CaSi_2$ to obtain the highest quality SiNSs.

Herein, we present a comparison of two different synthetic approaches for generating high purity $CaSi_2$, and thus, SiNSs (Scheme 1): (1) melting of elemental Ca and Si (denoted as EM-$CaSi_2$) and (2) the less-explored, solid-state hydride reaction between $CaH_2$ and Si (denoted as HS-$CaSi_2$). Our results show that the EM-$CaSi_2$ exhibits grains with large aspect ratios that lay flat against the substrate, whereas the HS-$CaSi_2$ has more uniform grains with little preferred orientation. These data suggest a preferential growth along the *a*- and *b*-axes of the EM-$CaSi_2$. We find that these morphological and crystallographic features are imparted onto the deintercalated SiNSs. Aside from the differing orientational crystallization of the $CaSi_2$ precursors, we demonstrate that all other properties of the precursor and deintercalated nanosheets are identical. Further, the HS-$CaSi_2$ pathway consists of a single step that does not require melting and crystallization of the $CaSi_2$ product and can be conducted at a temperature below the peritectic decomposition of $CaSi_2$. This work provides the field with a one-step approach for synthesizing high-purity $CaSi_2$ consisting of smaller and more uniform crystals with physical attributes that translate to the deintercalated SiNSs. These results are promising for photonic and optoelectronic applications as the smaller nanosheets should afford improved dispersibility which can be utilized for thin film deposition.

**Scheme 1. Two Different Synthetic Pathways for $CaSi_2$**[a]

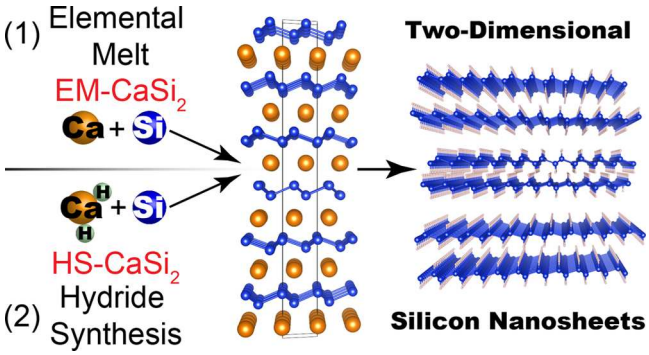


[a](1) Elemental melting of Ca and Si (EM-$CaSi_2$) and (2) the solid-state reaction between $CaH_2$ and Si, denoted as hydride synthesis (HS-$CaSi_2$), were compared and employed for the production of silicon nanosheets (SiNSs) via topotactic deintercalation. Both reaction pathways yield high-purity $CaSi_2$; however, the EM-$CaSi_2$ has a preferred growth orientation, a feature that translates to the deintercalated SiNSs, yielding sheets with large aspect ratios. Most importantly, the HS-$CaSi_2$ approach only requires a single heating step at a temperature below the melting point of $CaSi_2$, thus mitigating the potential peritectic decomposition while the reaction cools.

## METHODS

**$CaSi_2$ Synthesis.** *Elemental Melt Synthesis (EM-$CaSi_2$).* EM-$CaSi_2$ was synthesized by placing Si and Ca into a tantalum (Ta) tube, with slight stoichiometric excess silicon to prevent the formation of undesired phases (1:2.125 Ca:Si), and to replenish any consumed Si that reacts with the Ta tube. All work for the synthesis of $CaSi_2$ was performed in a glovebox filled with argon. In a typical synthesis, 2.991 g of Si pieces (Sigma-Aldrich 99.95%) and 2.008 g of Ca granules (Sigma-Aldrich 99%) were placed into a Ta tube (Eagle Alloys, the tube was cut to 3.25 inch long, with a 0.500 inch outer diameter and a 0.020 inch wall thickness). *Warning! The Ta tube must be long enough to avoid overpressurization of the tube! Overpressurization can cause tube failure and a sudden release of molten material! This reaction shall be performed inside an inert atmosphere, such as a glovebox!* The tube was crimped and welded shut using a gas tungsten arc welder (Miller Maxstar 210). The welded Ta tube was placed within the coil of an induction heater and heated until the contents melted together; the contents were kept molten for ∼1 min. Then, while the contents were still molten, the Ta tube was removed from the induction heater, immediately inverted, and allowed to cool for a few minutes until the contents solidified. This melting−inverting−cooling step was repeated for a grand total of four times. Finally, the contents were melted together once more, and while the contents were still molten, the Ta tube was placed into a container filled with aluminum chips to rapidly cool the product. The tube was then removed from the glovebox and rinsed with concentrated hydrochloric acid to remove aluminum that adhered to the exterior of the tube. Finally, the tube was rinsed with DI water, dried, transferred back into an Ar-filled glovebox, and opened to yield crystals of $CaSi_2$ that are typically 1−2 (up to ∼5) mm wide (Figure S1). Then, the $CaSi_2$ was ground in a mortar and pestle to yield crystallites that were ∼0.5 mm in size. The EM-$CaSi_2$ was stored under Ar or $N_2$ for use.

*Hydride Synthesis (HS-$CaSi_2$).* Silicon lumps (AlfaAesar, 99.9999%) were ground to a fine powder in a Plattner's mortar and pestle. Then, in an argon-filled glovebox, powders of $CaH_2$ (AlfaAesar, 98%) and Si were weighed in a molar ratio of $CaH_2$:Si = 1:2 and loaded into a polystyrene grinding vial equipped with a slip-on cap. After that, the vial was sealed inside two polypropylene bags under argon atmosphere, brought out of the glovebox, and ball-milled (8000 M MIXER/MILL) for 18 min. In the glovebox, the ball-milled powder was loaded in a Ta tube (Admat, ∼2 in. long, with a 0.375 inch outer diameter and a 0.020 inch wall thickness), which was then welded shut using a gas tungsten arc welder and placed into a silica reactor. The reactor was then evacuated down to $4 \times 10^{-5}$ bar. These reactors are equipped with Swagelok safety check valves to prevent overpressurization due to the release of $H_2$ gas during heat treatment. The reactor was then placed in a resistance furnace (Thermo Scientific Thermolyne type FD1500M) connected to thermocontrollers (Eurotherm 3216) and heated at a rate of 2.03 °C/min from room temperature to 1000 °C and held at 1000 °C for 24 h. After 24 h, the reactor was cooled to room temperature by switching off the furnace. The final product appeared as a fine black powder (Figure S1). The HS-$CaSi_2$ was stored under Ar or $N_2$ for use.

**SiNS Synthesis.** *Synthesis from EM-$CaSi_2$ Precursors.* In a glovebox filled with $N_2$, the $CaSi_2$ synthesized above by the elemental melt method (EM-$CaSi_2$) was ground using a mortar and pestle. Then, 3.05 g of the EM-$CaSi_2$ was placed in a vial and chilled to −35 °C under $N_2$ overnight. In a separate, 500 mL round-bottom three-necked flask, ∼305 mL of concentrated HCl was added, placed in the freezer, and chilled to −35 °C under flowing $N_2$ overnight. The next day, the $CaSi_2$ was added to the flask under a continuous flow of $N_2$. The reaction contents were allowed to sit unstirred at −35 °C for 11 days. After 11 days, the contents were filtered under $N_2$ atmosphere and washed with ∼250 mL of anhydrous methanol, followed by a final wash with ∼50 mL of anhydrous acetonitrile. Finally, the product was dried under vacuum for ∼80 h. The EM-SiNSs was stored under $N_2$ for additional characterization.

*Synthesis from HS-SiNSs Precursors.* The SiNSs synthesized from HS-$CaSi_2$ followed the same procedures as the synthesis of the EM-SiNSs except that (1) the $CaSi_2$ was not ground and (2) 0.245 g of $CaSi_2$ and 250 mL of HCl were used. The HS-$CaSi_2$ was not ground because the resulting product was already a fine powder. The HS-SiNSs were stored under $N_2$ for additional characterization.

**Structural and Optical Characterization.** *Powder X-ray Diffraction (pXRD).* pXRD data of both types of synthesized $CaSi_2$ precursors were collected with a Bruker DaVinci D8 Advance diffractometer with a Cu K$\alpha$ radiation source for the EM-$CaSi_2$ and a


https://doi.org/10.1021/acsanm.3c00001
ACS Appl. Nano Mater. 2023, 6, 10054−10063

Rigaku MiniFlex600 powder diffractometer with Cu K$\alpha$ radiation and Ni-K$\beta$ filter for the HS-$CaSi_2$. Rietveld refinement of both $CaSi_2$ pXRD patterns was conducted with GSAS-II crystallography data analysis software.[25]

*Total X-ray Scattering.* Total scattering data were collected at the Advanced Photon Source (APS), Argonne National Laboratory at the 11-ID-B beamline with a 2D detector at two distances: 180 and 1000 mm. Pair distribution function (PDF) data were derived from the data associated with the 180 mm distance ($Q_{max} \approx 24$ Å$^{-1}$), while the azimuthally integrated synchrotron powder X-ray diffraction (AI-spXRD) data were derived from the data associated with the 1000 mm distance. An X-ray energy of 86 720 eV was used. The 2D total scattering data were azimuthally integrated with the GSAS-II software[25] after calibrating to a $CeO_2$ standard to obtain synchrotron total X-ray scattering data. The PDF was extracted with the PDFgetX2 software[26] by first subtracting an independently collected polyimide background. Structural refinement was performed with the PDFgui software.[27]

*Fourier-Transform Infrared Spectroscopy (FTIR).* FTIR data were collected with a Nicolet iS5 FTIR spectrometer with an iD5 attenuated total reflectance (ATR) accessory.

*Raman.* Raman data were collected using a WITec alpha300R confocal Raman microscope system. The wavelength of the incident laser was 532 nm, and the objective lens was 100× with ~1 $\mu$m diameter spot size. The laser power was kept below ~0.3 mW to minimize potential damage to the SiNSs.

*Solid-State NMR Spectroscopy.* Solid-state NMR spectroscopy experiments were performed on a 9.4 T ($\nu_0(^1H)$ = 400 MHz) Bruker wide-bore magnet spectrometer equipped with a Bruker Avance III HD console and a 4 mm magic-angle spinning (MAS) HXY NMR probe configured in double resonance mode. All SiNSs were packed into 4 mm zirconia NMR rotors inside an Ar-filled glovebox, and the NMR rotors were spun with $N_2$ gas to avoid oxygen and moisture exposure. $^1$H chemical shifts were referenced to 1% tetramethylsilane (TMS) in $CDCl_3$ with adamantane ($\delta(^1H)$ = 1.7 ppm) as a secondary chemical shift reference. $^{29}$Si chemical shifts were indirectly referenced using previously published IUPAC recommended relative NMR frequencies.[28] All NMR spectra were initially processed and referenced using the Topspin 3.6.1 software. Car−Purcell−Meiboom−Gill (CPMG) echo trains were coadded using the NUTs NMR processing software (Acorn, Inc.). All solid-state NMR spectroscopy experimental details (MAS frequency, recycle delay, number of scans, $t_1$ dwell ($\Delta t_1$), $t_1$ TD points, CP contact time/$J$-evolution time, and total experimental times) are given in Table S1. The $^1$H $\pi/2$ and $\pi$ pulse durations were 2.5 and 5.0 $\mu$s in duration, corresponding to a 100 kHz radio frequency (RF) field. $^{29}$Si $\pi/2$ and $\pi$ pulse durations were 5.0 and 10.0 $\mu$s in duration, corresponding to a 50 kHz RF field. Direct excitation $^{29}$Si NMR spectra were recorded utilizing a rotor synchronized spin echo NMR pulse sequence with a 10 kHz MAS frequency. All $^1$H−$^{29}$Si heteronuclear correlation (HETCOR) NMR experiments, cross-polarization (CP) and scalar-based insensitive nuclei enhanced by polarization transfer ($J$-INEPT), were recorded with a 8.928 kHz MAS frequency, 100 kHz $^1$H RF field of eDUMBO$_{1-22}$ homonuclear dipolar decoupling[29] during the indirect acquisition of $^1$H and during $J$-evolution periods (if applicable), and Car−Purcell−Meiboom−Gill (CPMG)[30] detection for the direct acquisition of $^{29}$Si (24 rotor cycles per half echo, 8 total echoes). 100 kHz $^1$H RF field of SPINAL-64 heteronuclear decoupling was performed during the direct acquisition of $^{29}$Si.[31] $^1$H → $^{29}$Si CP was achieved with simultaneous $^1$H and $^{29}$Si spin-lock pulses: ~57 kHz $^1$H RF field (90−100% ramp) and ~48 kHz $^{29}$Si RF field.

*Transmission Electron Microscopy (TEM) and Electron Diffraction.* TEM images were recorded using an FEI Tecnai G2-F20 instrument operated at 200 kV. Samples for TEM were prepared by sonicating in degassed, anhydrous toluene before depositing on lacey carbon grids in a glovebox filled with $N_2$.

*Scanning Electron Microscopy (SEM).* SEM images were acquired with a FEI Quanta 250 field-emission scanning electron microscope. Samples were prepared in a glovebox filled with $N_2$ by either painting an aluminum SEM pin stub (Ted Pella, Inc., no. 16111) with carbon paint (Ted Pella, Inc., no.16053) or affixing a double coated, high purity conductive carbon Spectro tab (Ted Pella, Inc., no. 16084-4) atop the pin stub, followed by sample deposition onto the carbon supports. Specifically, a small quantity (approximately 5−10 mg) of dried SiNS sample was placed on a sheet of weighing paper and uniformly spread out across an area of roughly 1.5 cm$^2$. The carbon covered pin stub was then carefully pressed against the sample (in the case of the carbon paint, while the paint was still wet) until the desired level of sample coverage was achieved. The stubs were transferred to glass vials with an SEM pin mount gripper and were lightly tapped against the vial wall to knock off any loosely adhered sample. To minimize the potential for oxygen exposure during transportation to the characterization facility, the threads of the vials were wrapped with at least three full rotations of PTFE plumber's tape prior to capping. After capping, three full rotations of electrical tape were wrapped around the cap/vial interface. For samples deposited on carbon paint, the paint was allowed to dry before sealing the stub in a vial. The vials were kept in the glovebox until needed and in the $N_2$-filled vials until immediately before loading into the SEM. Additionally, the sample-coated stubs were briefly blown off with compressed air prior to loading to further remove any loosely adhered SiNSs. During the loading and instrument preparation process, samples were exposed to air for no more than 10 min. The instrument was operated at an electron accelerating voltage of 10 kV, and the samples were characterized in low vacuum mode with a water vapor pressure of 40−60 Pa to minimize charging effects.

*Diffuse Reflectance.* Diffuse reflectance of the SiNSs was collected with a PerkinElmer Lambda 750 equipped with a Labsphere 100 mm integrating sphere. To collect diffuse reflectance data, the SiNS samples were dispensed onto the adhesive side of transparent, colorless packaging tape (3M Scotch packaging tape), and reflectance was collected of the exposed SiNSs. The reflectance data were then transformed into the Kubelka−Munk function.[32]

*Steady-State Photoluminescence (PL).* PL excitation and emission spectra were acquired with a PerkinElmer LS 55 fluorescence spectrometer employing emission and excitation wavelengths of 525 and 370 nm, respectively. Suspensions were made at a concentration of 0.5 mg mL$^{-1}$ in methanol.

*Time-Resolved Photoluminescence (TRPL).* All TRPL data were collected with a Horiba DeltaFlex TCSPC and an excitation wavelength of 359 nm and monitored at 510 nm with a slit width of 32 nm. The decay was fit to the following equation: $I(t) = Ae^{-t/\tau_1} + Be^{-t/\tau_2} + Ce^{-t/\tau_3}$, where $A$, $B$, $C$, $\tau_1$, $\tau_2$, and $\tau_3$ are fitting parameters.

**Computational Methods.** *Density Functional Theory (DFT).* DFT calculations were performed with VASP.[33,34] The exchange−correlation functionals were described by the PBE-GGA.[35] PAW potentials[33,36,37] approximated the core electrons. The entire unit cell shape, volume, and atomic positions were relaxed until all forces and the self-consistent field energies were less than 0.01 eV/Å and $10^{-5}$ eV, respectively, and the kinetic energy cutoff was 550 eV. The Brillouin zone was sampled with a $k$-point density of 8 points/Å$^{-1}$ with a Monkhorst−Pack grid.[38]

## RESULTS AND DISCUSSION

A common approach for synthesizing $CaSi_2$ as a precursor to SiNSs has been to combine elemental sources of Ca and Si and subsequently melt them together to yield $CaSi_2$ (eq 1).[39−41] Another promising yet far less-utilized approach for synthesizing $CaSi_2$ is through the reaction of $CaH_2$ and Si (eq 2). The first reported synthesis of $CaSi_2$ from the reaction of $CaH_2$ and Si was by L. Wöhler and F. Müller in 1921;[42] however, to the best of our knowledge, there have been no reports that compare the properties of the SiNSs derived from these two $CaSi_2$ precursors. Unlike the melt-based synthesis, the hydride-based synthesis mitigates the potential for phase segregation, as it employs a reaction temperature of 1000 °C, which is below the temperature at which peritectic decomposition is expected


https://doi.org/10.1021/acsanm.3c00001
ACS Appl. Nano Mater. 2023, 6, 10054−10063

to occur (1030 °C).[40,43,44] Synthesis of HS-$CaSi_2$ at lower temperatures (without melting) is facilitated by the enhanced diffusion aided by intimate mixing between silicon and the salt-like $CaH_2$ precursor. The hydride-based synthesis has been extensively utilized to prepare doped and undoped $Na_4Si_4$ and $Na_4Ge_4$ as precursors in the solution synthesis of Si and Ge quantum dots.[45−52] We refer to products derived from the hydride synthesis with the prefix "HS" and products derived from the elemental-melt route with "EM".

$$\mathrm{Ca} + 2\mathrm{Si} \xrightarrow{\text{melt}, T>1150\ ^\circ\mathrm{C}} \mathrm{CaSi_2} \quad (\mathrm{EM}) \tag{1}$$

$$\mathrm{CaH_2} + 2\mathrm{Si} \xrightarrow{1000\ ^\circ\mathrm{C}} \mathrm{CaSi_2} + \mathrm{H_2}\uparrow \quad (\mathrm{HS}) \tag{2}$$

We characterized the phase purity of the $CaSi_2$ products using powder X-ray diffraction (pXRD) (Figure 1a). Upon

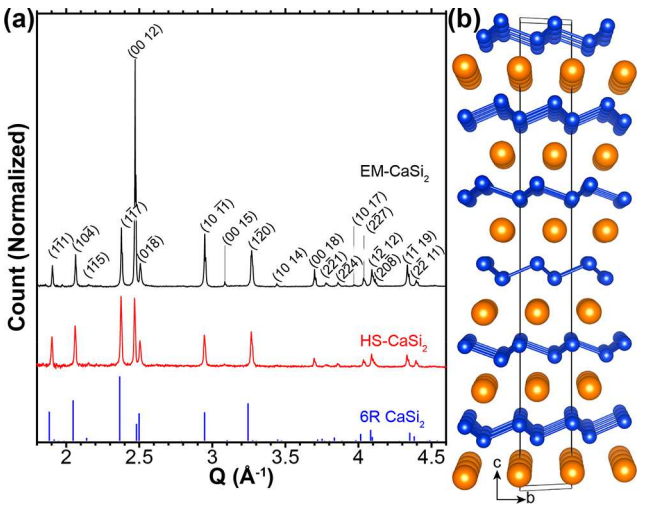


**Figure 1.** (a) Powder X-ray diffraction patterns of $CaSi_2$ synthesized from the elemental melt synthesis (EM-$CaSi_2$, black, top) and the hydride synthesis (HS-$CaSi_2$, red, middle). The reference pattern at the bottom (blue) corresponds to the 6R phase of $CaSi_2$ (PDF no. 01-083-6182). The data were normalized to the peak at $Q \approx 3.25$ Å$^{-1}$. (b) Ball and stick model of 6R $CaSi_2$. Silicon atoms are shown in blue with Si−Si bonds, and Ca ions are shown in orange.

comparing the pXRD patterns of the EM-$CaSi_2$ and HS-$CaSi_2$, we find that both pXRD patterns resemble the 6R phase of $CaSi_2$. The 6R phase of $CaSi_2$ contains six Si sheets per unit cell, where each sheet exhibits a $a \times (^1/_3)$ and $b \times (^2/_3)$ translational shift and a 30° rotation relative to the sheet below it (Figure 1b).[53,54] We find that the reflection corresponding to the (00 12) plane of the EM-$CaSi_2$ has a much greater relative intensity than in the HS-$CaSi_2$. Furthermore, the intensity of this peak is greater than that of the powder reference pattern, indicating that the *c*-axis of the EM-$CaSi_2$ preferentially points perpendicular to the substrate used for pXRD measurements. This preferred orientation likely arises from a larger aspect ratio in the EM-$CaSi_2$ relative to the HS-$CaSi_2$, where the dimensions of the $CaSi_2$ crystallites along the *a*- and *b*-directions are larger than the dimensions along the *c*-direction. We attribute this aspect ratio to a preferential growth along the *a*- and *b*-axes when using the EM synthetic technique or from preferential cleavage of $CaSi_2$ grains during the grinding process, giving rise to plate-like grains that lay flat against the substrate.[55] We note that the preferred orientation was reproducible among seven consecutive syntheses. Indeed, upon normalizing both pXRD patterns to the reflection corresponding to the $(1\bar{2}0)$ plane of 6R $CaSi_2$ (the only prominent reflection that does *not* contain contributions from the $\{hkl\}$ (for which $l > 0$) set of planes), the preferred orientation with the *c*-axis perpendicular to the substrate becomes apparent (Figure 1a). The preferred orientation is the only discernible microstructural difference between the two products. Rietveld refinement of the pXRD data shown in Figure 1 confirms that the synthesized precursors were indeed 6R $CaSi_2$ (Figure S2 and Table S1). Additionally, accounting for the preferred orientation in the refinement of EM-$CaSi_2$ led to a markedly improved fit, further corroborating the suspected preferential growth; however, even after multiple refinement attempts, the preferential orientation still could not be closely modeled, as evidenced by the difference plot, leading to higher-than-desired residual values. The EM- and HS-$CaSi_2$ powders also had a different macroscopic appearance, with the EM-$CaSi_2$ consisting of particles that are approximately 1−2 mm in size and the HS-$CaSi_2$ consisting of a very fine powder (Figure S1). However, we find that the Scherrer grain size for EM- and HS-$CaSi_2$ is 0.56 and 0.44 $\mu$m, respectively. This suggests that the larger particle size of the EM-$CaSi_2$ is comprised of crystal aggregates.

After confirming that both synthetic routes yield 6R $CaSi_2$, we then synthesized SiNSs via the deintercalation of Ca from $CaSi_2$ in concentrated aqueous HCl at −35 °C. Such conditions were chosen to achieve the highest extent of hydrogen termination possible (i.e., $Si_6H_6$, also known as silicane or layered polysilane) since it has been reported that deintercalation temperatures above 0 °C result in substantial oxygen content,[1,56] producing a product more reminiscent of the historically reported siloxenes ($Si_6H_3(OH)_3$),[2−5] while temperatures below approximately −20 °C yield nearly 80% hydrogen termination with the remaining surface being predominately functionalized by chlorine (up to 20%) and oxygen (<10%).[21,57] Note that a colder deintercalation temperature was not employed as the reaction mixture would likely solidify since the freezing point of concentrated HCl (36.5−38.0%) is approximately −30 °C; our deintercalations did not freeze even though the reported freezing point of concentrated HCl is higher than the employed deintercalation temperature.

We characterized the SiNSs with azimuthally integrated synchrotron powder X-ray diffraction (AI-spXRD) at Argonne National Lab (Figure 2). The AI-spXRD data indicate that the SiNSs derived from the two precursors have nearly identical structures, with the only exception being that the EM-SiNSs exhibit an increased intensity of the reflection corresponding to the (006) plane relative to the HS-SiNSs, indicative of preferred orientation along the *c*-axis. This preferred orientation is expected given that the EM-$CaSi_2$ precursor also demonstrated a structurally similar preferred orientation. Ball and stick models of the SiNSs viewed down the *c*- and *a*-axes are provided in Figure 2b and Figure 2c, respectively, for reference. Note that the unit cell of the SiNSs contains six sheets per unit cell, and as such, the *d*-spacing associated with the (006) plane corresponds to the intersheet spacing.[58] The AI-spXRD also shows very small features that correspond to residual $TaSi_2$ at $Q \approx 2.8$ Å$^{-1}$ (Figure S3), which is formed during the synthesis of $CaSi_2$. The formation of small quantities of $TaSi_2$ is typical when performing reactions in sealed tantalum tubes.[52] Notably, $TaSi_2$ is not detected with pXRD using a laboratory diffractometer in either the EM-$CaSi_2$


https://doi.org/10.1021/acsanm.3c00001
ACS Appl. Nano Mater. 2023, 6, 10054−10063

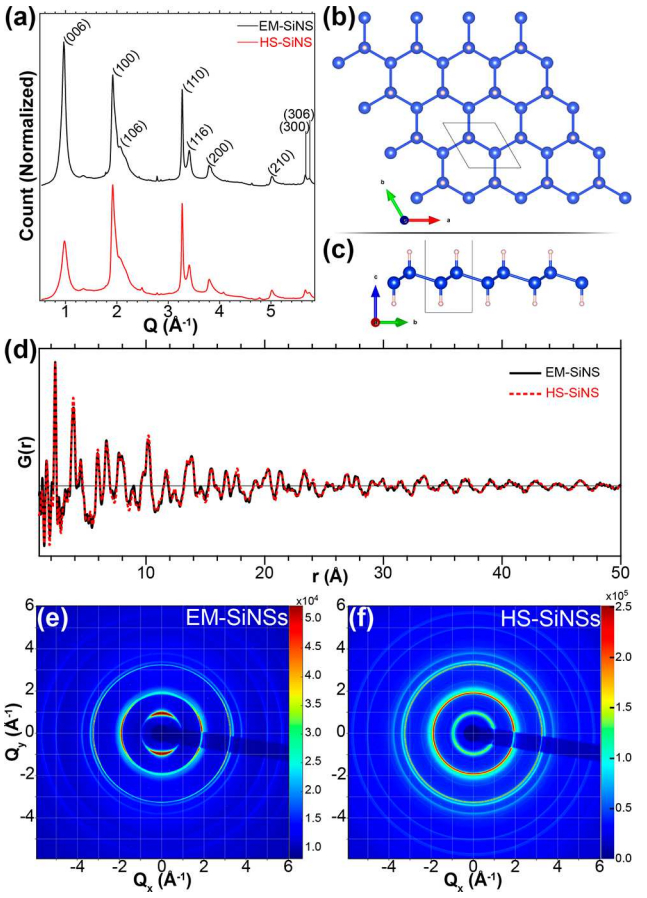


**Figure 2.** X-ray structural characterization of SiNSs. (a) AI-spXRD of the deintercalated SiNSs. Ball and stick models of the SiNSs viewed (b) down the *c*-axis and (c) down the *a*-axis. Blue and white atoms correspond to silicon and hydrogen, respectively. (d) Atomic pair distribution function (PDF) of the deintercalated SiNSs. Panels (e) and (f) are the 2D X-ray scattering patterns for the EM-SiNSs and HS-SiNSs, respectively.

or HS-$CaSi_2$ precursors, and its presence only became apparent when using synchrotron X-ray sources. This suggests that $TaSi_2$ exists in very low concentrations and is further supported because the diffraction intensity of crystalline $TaSi_2$ is expected to be much larger than the paracrystalline SiNSs. We previously determined that the SiNSs exhibit a large degree of disorder along the *c*-axis, thereby decreasing the overall scattering intensity relative to highly crystalline materials.[58] As a rough means to quantify the amount of $TaSi_2$ in the SiNSs, we took the ratio of the area of the most intense AI-spXRD peak corresponding to $TaSi_2$ to that of the area of the peaks spanning 3−3.6 $Å^{-1}$ in Figure 2a; we find that this ratio is 0.017 and 0.036 for EM-SiNSs and HS-SiNSs, respectively. Thus, we conclude there is a very low concentration of $TaSi_2$. It should be noted that $TaSi_2$ contamination in the HS-$CaSi_2$ synthesis can, in principle, be avoided if the precursor powders are loaded into an alumina boat inside a silica reactor in the flow-furnace, as was previously done for the synthesis of $Na_4Si_4$.[45]

The AI-spXRD in Figure 2a probes crystallographic periodicity, but it is limited in its usefulness for disordered materials. To better understand the structure of the SiNSs, we turned to the atomic pair distribution function (PDF) analysis of the total X-ray scattering data to identify the local and long-range structure within the samples. Our X-ray PDF results indicate that the SiNSs are nearly indistinguishable from each other, implying that both the long- and short-range structure of the EM-SiNSs are nearly identical to that of the HS-SiNSs for length scales up to ∼50 Å (Figure 2d).

Despite the similarity in the PDF data, the 2D X-ray scattering data (Figure 2e,f) of SiNSs packed in capillaries reveal distinct differences in the orientation of the samples with respect to the incident beam. The EM-SiNSs displayed a strong scattering along $Q_X = 0$ (the vertical axis) and $Q_Y = 0$ (the horizontal axis); in contrast, scattering from the HS-SiNSs was independent of the azimuthal angle. This suggests that the HS-SiNSs do not exhibit preferred orientation with respect to the incident beam, unlike the EM-SiNSs. We suspect that this long-range preferred orientation with respect to the incident X-rays in EM-SiNSs is a result of packing the capillaries, where the EM-SiNSs have a plate-like aspect ratio and tend to stack with their normal vector parallel to the axis of the capillary.[58] In contrast, the HS-SiNSs exhibit a smaller aspect ratio and do not have a preferred orientation. We liken this preferred orientation of the EM-SiNSs to how playing cards stack when dropped onto a table.[55] A detailed analysis of the preferred orientation in the EM-SiNSs can be found in our previous work.[58]

Scanning electron microscopy (SEM) images of the SiNSs (Figure S4) reveal sample morphologies of loosely stacked sheets, indicative of $Ca^{2+}$ deintercalation, and is consistent with our previous work.[21,58] Most importantly, these imaging studies corroborate the conclusions drawn from the diffraction studies; that is, the EM-SiNSs exhibit large plate-like structures with larger aspect ratios stemming from preferential growth of the $CaSi_2$ precursor along the *a*- and *b*-axes. Specifically, the EM-SiNSs consist of a heterogeneous population of sheets (and stacks thereof), often presenting with lateral dimensions in excess of 100 $\mu$m (Figure S4a,b), whereas the HS-SiNSs consist of a fairly uniform population of sheet stack size with more homogeneous and substantially smaller lateral dimensions not exceeding approximately 40 $\mu$m (Figure S4d,e). This marked difference in aspect ratio accounts for the EM-SiNSs tendency to preferentially stack with the *c*-axis perpendicular to a substrate while the HS-SiNSs show no preference, as their uniform size affords more efficient, albeit random, packing. We note, at higher magnification, the stacks of sheets are similar in appearance (Figure S4c,f), as expected, although the difference in lateral dimensions is still quite apparent as almost the entire sheet stack is visible for the HS-SiNSs (panel f) whereas only a corner of the stack fits in the field of view for the EM-SiNSs (panel c).

To characterize the molecular structure of the SiNSs, we used FTIR and Raman spectroscopy (Figure 3). The vibrational modes in the FTIR spectra include SiH at 2092, 737, 633, and 507 $cm^{-1}$; SiOH at 3600 and 900 $cm^{-1}$; SiO at 1177 and 1019 $cm^{-1}$; $O_XSiH$ at 792 $cm^{-1}$; and SiCl at 571 $cm^{-1}$ (Figure 3a).[21,58] We find a one-to-one correspondence in the FTIR peaks for EM-SiNSs and HS-SiNSs. There are differences in relative peak intensities; however, it is important to note that the FTIR background signal makes it difficult to compare FTIR peak intensities, particularly in the fingerprint region, where the EM-SiNSs exhibit a more intense background. Most notably, we find that the $O_XSiH$ mode at ∼800 $cm^{-1}$ in the HS-SiNSs is more intense than in the EM-SiNSs. We previously quantified the relative sensitivity of different IR modes in SiNSs[21] and found that FTIR is extremely sensitive


https://doi.org/10.1021/acsanm.3c00001
ACS Appl. Nano Mater. 2023, 6, 10054−10063

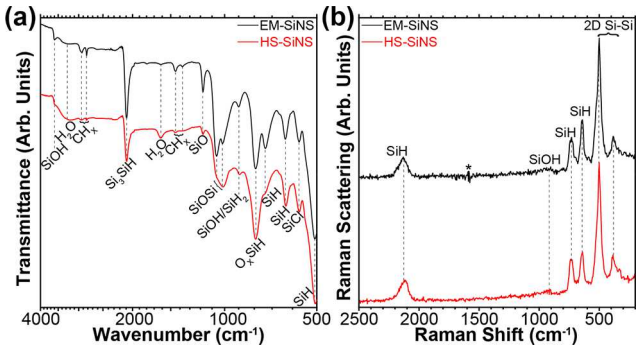


**Figure 3.** Vibrational characterization of SiNSs. (a) FTIR of the deintercalated SiNSs with labeled peaks. Note that the *x*-axis is on a logarithmic scale to aid in visualizing the peaks in the fingerprint region. (b) Raman spectra of the SiNSs. The asterisk (*) corresponds to the substrate (highly oriented pyrolytic graphite, HOPG). All vertical dashed lines are to guide the eye.

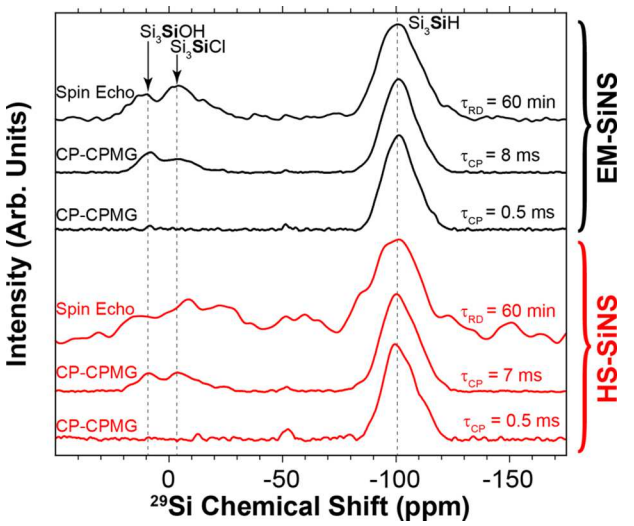


**Figure 4.** $^{29}$Si SSNMR spectra of SiNSs. Comparison of 1D direct excitation $^{29}$Si spin echo and $^{1}$H → $^{29}$Si CP-CPMG NMR spectra of EM-SiNSs (upper, black) and HS-SiNSs (lower, red) acquired with 10 kHz MAS.

to vibrational modes associated with Si−O bonds. The observed differences in the FTIR intensities of these samples likely arise from small differences in the synthesis, preparation, and morphology of the SiNSs and $CaSi_2$. We note that all peaks present in the data presented here were also present in our previous study that used commercially available $CaSi_2$;[21] however, the relative intensities of the features differ, with these samples having less contributions from SiOSi. This is likely a result of the washing procedure, where the EM- and HS-SiNSs were washed under an inert atmosphere, and the SiNSs derived from commercially available $CaSi_2$ were washed under ambient conditions.[21]

Raman spectroscopy is often used to characterize silicon nanomaterials; the location and shape of the Si−Si feature at ∼500 $cm^{-1}$ are used to infer crystallinity.[59,60] The EM-SiNSs and HS-SiNSs exhibit nearly identical Si−Si modes with a peak position for both samples residing at 500 $cm^{-1}$ (Figure 3b). In addition, the relative intensities of all of the SiH (approximately 640, 730, and 2120 $cm^{-1}$), SiOH (∼930 $cm^{-1}$), and Si−Si (approximately 500 and 380 $cm^{-1}$) Raman modes are nearly indistinguishable between the samples, indicating that the EM-SiNSs and HS-SiNSs have similar bonding, crystallinity, and surface termination. We note that the Raman spectra presented here are nearly identical to the Raman spectra obtained from SiNSs derived from commercially available $CaSi_2$ except that these spectra do not contain signals from the bulk silicon impurity present in commercially available $CaSi_2$.[21]

Next, $^{1}$H and $^{29}$Si solid-state NMR (SSNMR) spectroscopy was used to further probe the molecular structure of the EM- and HS-SiNSs. The one-dimensional (1D) $^{1}$H → $^{29}$Si cross-polarization magic-angle spinning (CPMAS; through-space) SSNMR spectra of EM- and HS-SiNSs (acquired with Car−Purcell−Meiboom−Gill (CPMG)[30] for $^{29}$Si detection) are nearly identical (Figure 4), corroborating our assessment above that the two SiNSs have nearly indistinguishable local molecular structures. Notably, the direct excitation MAS $^{29}$Si spin echo NMR spectra do not reveal NMR signals at −80 ppm from bulk Si impurities that were previously observed when SiNSs were synthesized from commercially available (technical grade) $CaSi_2$;[21] however, the features that do correspond to the SiNSs are similar to our previous study.[21] Based on our prior study, we assign the $^{29}$Si NMR signals at approximately −100 ppm to $Si_3$**Si**H species.[21] This assignment was confirmed by monitoring the evolution of the 1 bond $^{1}$H−$^{29}$Si *J*-coupling ($^{1}J_{H-Si}$) under $^{29}$Si magnetization and also by recording 2D $^{1}$H → $^{29}$Si scalar INEPT (*J*-INEPT; through-bond) and CP heteronuclear correlation (HETCOR) NMR spectra (Figures S5 and S6, respectively).[21,61,62] Notably, the 1D $^{1}$H → $^{29}$Si CPMAS and direct excitation $^{29}$Si NMR spectra in Figure 4 reveal two additional NMR signals at approximately 10 and −5 ppm. Our prior DFT calculations predicted that $Si_3$**Si**OH and $Si_3$**Si**Cl groups resonate at $^{29}$Si chemical shifts of approximately 24−32 and 15−24 ppm, respectively.[21] Therefore, we tentatively assign the $^{29}$Si NMR signals at 10 and −5 ppm to $Si_3$**Si**OH and $Si_3$**Si**Cl, respectively. The unambiguous identification of both $Si_3$**Si**OH and $Si_3$**Si**Cl species is ongoing in our lab.

We characterized the microstructure of the SiNSs with bright field transmission electron microscopy (TEM) and electron diffraction (ED), as shown in Figure 5. The TEM images demonstrate the SiNSs consist of stacks of very thin sheets. The morphology of the sheets is very similar between the two samples. We note that the high-contrast debris (dark spots) that was present in the EM-SiNSs shown in Figure 5a was also observed while imaging the HS-SiNSs but is not present in Figure 5b. We suspect that these dark spots are either small fragments of SiNSs or $TaSi_2$. Additionally, we find that large, continuous flakes were qualitatively more frequent in the EM-SiNSs sample.

The ED patterns viewed down the [001] zone axis of both samples are shown in Figure 5c,d. We find that both samples exhibit bright spots in a hexagonal arrangement, in addition to lower-intensity diffuse hexagons. Though these diffuse hexagons are more prevalent in the EM-SiNSs, they are indeed present within HS-SiNSs as well. Trout et al. observed a similar ED pattern in germanane and attributed these diffuse hexagons to turbostratic twisting along the *c*-axis.[63] It is possible that turbostratic twisting could be present in these TEM samples; however, the AI-spXRD data and our previous analysis[58] make it clear that SiNSs are well-registered from sheet-to-sheet, as is made apparent by the sharp peak corresponding to the (110) plane (Figure 2a). Alternatively, the diffuse hexagons could arise from disorder within the unit


https://doi.org/10.1021/acsanm.3c00001
ACS Appl. Nano Mater. 2023, 6, 10054−10063

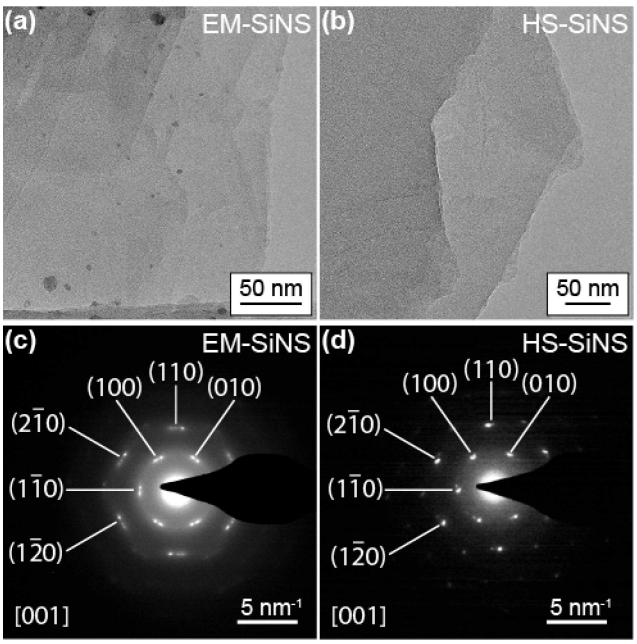


**Figure 5.** (a) and (b) are TEM images of the EM-SiNSs and HS-SiNSs, respectively. (c) and (d) are indexed electron diffractograms viewed down the [001] zone axis for the EM-SiNSs and HS-SiNSs, respectively.

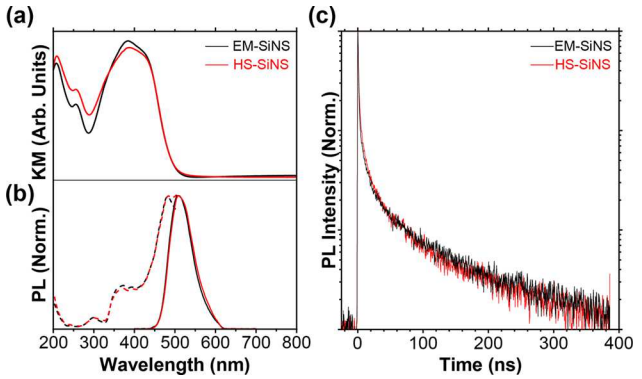


**Figure 6.** Optical characterization of the deintercalated SiNSs. (a) Kubelka–Munk transformation of diffuse reflectance data, (b) steady-state photoluminescence, and (c) single-wavelength, time-resolved photoluminescence decays. In panel (b), excitation spectra (dashed lines) were collected at an emission wavelength of 525 nm while the emission spectra (solid lines) were collected at an excitation wavelength of 370 nm. For collection of the PL decays shown in panel c, the samples were excited at 359 nm and emission was monitored at 510 nm.

cell of isolated, individual nanosheets. Welberry demonstrated that deviations within the lattice vector direction within a plane of atoms can lead to these diffuse hexagons.[64] Given the sharp (110) diffraction planes in the AI-spXRD, we conclude that the diffuse hexagons observed in Figure 5c,d arise from variations of the unit cell lattice vector direction within an isolated nanosheet. Moreover, we find that both EM- and HS-SiNSs are very sensitive to the beam, with the ED patterns transforming into diffuse rings over the course of a few seconds (Figure S7). We attribute this transformation of the ED signal into diffuse rings to be a result of the amorphization of the Si framework; this beam-induced amorphization exhibits similar structural and temporal responses to germanane.[63] Given that this beam-induced amorphization occurs on such short time scales, it is difficult to conclusively determine if the diffuse hexagons are true structural characteristics of the samples or are a result of beam-induced deviations within the lattice vectors; additionally, it makes it difficult to accurately compare the ED pattern associated with the EM- and HS-SiNSs.

Both EM- and HS-SiNSs exhibit satellite diffraction spots within the ED pattern that we attribute to shear lines in a stack of nanosheets, whereby each half of the shear line exhibits a small degree of rotation relative to each other. We find that both AI-spXRD and the ED patterns are consistent with a hexagonal unit cell with a unit cell lattice parameter $a$ = 3.84 Å. Our DFT calculations predict a lattice parameter of 3.89 Å (Figure S9); this overestimation of the DFT parameter is 1.3% and is similar to the ∼0.7% increase in lattice constant that is found when comparing the DFT lattice parameters of bulk Si. This overestimation is a common occurrence for the PBE functional.[65]

We characterized the optical properties of the SiNSs with diffuse reflectance and steady-state photoluminescence (PL) spectroscopies, as well as single-wavelength, time-resolved photoluminescence (TRPL) decays, as shown in Figure 6. The diffuse reflectance data were transformed into the Kubelka–Munk function (KM),[32] which is analogous to absorbance and is regularly used for highly scattering samples. The KM functions of both samples have a sharp onset beginning at ∼500 nm and are similar in their spectral features (Figure 6a). Relative to the HS-SiNS, the EM-SiNSs exhibit a larger intensity at the peak centered at ∼400 nm and weaker intensity at the peak centered at ∼200 nm. DFT simulations of the extinction coefficient (Figures S8 and S9) of H-terminated SiNSs demonstrate that the peak in the KM at ∼400 nm originates from a dielectric response arising from an electric field applied in-plane to the SiNSs (i.e., along the $a$- or $b$-axes). Conversely, the peak at ∼200 nm arises from a dielectric response due to an electric field applied out-of-plane to the SiNSs (i.e., along the $c$-axis). Thus, the differences in relative absorbance of these features within the experimental SiNSs can be explained by the orientations of the samples with respect to the incident light beam. The EM-SiNSs (consisting of sheets that preferentially lay with their $c$-axes parallel to the incident beam) will experience a greater electric field in-plane compared to a randomly oriented sample. Thus, the EM-SiNSs are expected to exhibit higher intensity at ∼400 nm and lower intensity at ∼200 nm compared to the randomly oriented HS-SiNSs, as is observed in Figure 6a.

Both of the SiNS samples have a PL emission peak that is centered at ∼508 nm (∼2.44 eV), with an identical fwhm of 0.32 eV (Figure 6b; solid lines). This is consistent with our previous report, which used a commercially available $CaSi_2$ precursor.[21] Similarly, both samples have nearly identical excitation spectra that have four main features (Figure 6b; dashed lines): (i) decreasing emission from 200 to 250 nm, (ii) a small peak centered at ∼300 nm, (iii) a large shoulder between 340 and 400 nm, and (iv) the maximal peak centered at 478 nm. The poor correlation between the excitation spectra and KM pseudoabsorbance is not at all surprising given the highly scattering nature of the SiNS dispersions. Further, the excitation (and emission) spectra were not corrected for instrumental factors, which is likely playing a role in the observed peak positions and intensities. Regardless, the excitation and emission spectra for the EM- and HS-SiNSs are highly consistent between the two approaches, indicating


https://doi.org/10.1021/acsanm.3c00001
ACS Appl. Nano Mater. 2023, 6, 10054−10063

that the differing synthetic approaches for $CaSi_2$ and resulting morphological differences in the SiNSs do not markedly impact the photophysical properties (e.g., ground and excited states) of the material. We fit the TRPL data (Figure 6c) to a triexponential decay, as Si nanomaterials often require multiexponential or stretched exponential decays.[66−68] However, the lifetimes that we observe are notably shorter than most Si nanomaterials (e.g., Si nanocrystals). Our TRPL lifetimes (exponential coefficients) are 0.65 ns (0.87), 6.3 ns (0.11), and 61 ns (0.2). These short lifetimes suggest direct emission.[63] Importantly, both steady-state and time-resolved photoluminescence data were collected from dispersions in methanol, so any effects of preferred orientation were not detected.

## CONCLUSION

We compare the properties of $CaSi_2$ synthesized by two separate reaction pathways and silicon nanosheets (SiNSs) derived therefrom. These reaction pathways involve the conventional technique of melting together elemental Ca and Si, and the less-explored reaction between calcium hydride and elemental bulk silicon. We find that the $CaSi_2$ powder that is derived from the hydride-based synthesis (HS-$CaSi_2$) has a nearly identical structure to $CaSi_2$ derived from conventional melting of elemental precursors (EM-$CaSi_2$). However, EM-$CaSi_2$ powders exhibit preferred orientation with the *c*-axis perpendicular to the substrate, whereas the HS-$CaSi_2$ powder has very little preferred orientation. This suggests that the EM-$CaSi_2$ has a larger aspect ratio which may arise from preferential growth along the *a*- and *b*-axes when using the EM synthetic technique or from preferential cleavage of $CaSi_2$ grains during the grinding process. We then deintercalated both $CaSi_2$ precursors to form atomically thin SiNSs and compare their properties. We found that the orientation of the precursor (or lack thereof) is imparted to the SiNSs that are formed upon deintercalation. Using total-scattering X-ray diffraction, pair distribution function analysis, FTIR, Raman, solid-state NMR spectroscopy, TEM, electron diffraction, diffuse reflectance spectroscopy, PL, and TRPL, we demonstrate that both SiNS samples have nearly identical microstructural and optical properties. The only discernible difference between the SiNS samples is that the EM-SiNSs exhibit small differences in the absorbance spectrum that can be attributed to orientation-dependent differences in extinction coefficient. These results provide the community with a convenient method for synthesizing high-purity $CaSi_2$ in a single step that requires lower temperatures than the commonly used methods. Furthermore, the nanosheets obtained through the deintercalation of the HS-$CaSi_2$ should show promise in next-generation photonics and optoelectronics since the smaller, more uniform sheets can be more readily dispersed in an appropriate solvent which will yield more optically transparent films, a prerequisite for such target applications.

## ASSOCIATED CONTENT

### Supporting Information

The Supporting Information is available free of charge at https://pubs.acs.org/doi/10.1021/acsanm.3c00001.

Photograph of $CaSi_2$ crystals, XRD and lattice constants, SEM images, SSNMR spectra, SSNMR pulse sequences, SSNMR evolution curves, electron diffraction, and DFT simulations of direction-dependent extinction coefficient (PDF)

## AUTHOR INFORMATION


### Corresponding Author

**Matthew G. Panthani** − *Department of Chemical and Biological Engineering, Iowa State University, Ames, Iowa 50011, United States;* orcid.org/0000-0002-3795-2051; Email: panthani@iastate.edu

### Authors

**Bradley J. Ryan** − *Department of Chemical and Biological Engineering, Iowa State University, Ames, Iowa 50011, United States;* orcid.org/0000-0002-7719-5593

**Gourab Bhaskar** − *Department of Chemistry, Iowa State University, Ames, Iowa 50011, United States*

**Jeremy B. Essner** − *Department of Chemical and Biological Engineering, Iowa State University, Ames, Iowa 50011, United States;* orcid.org/0000-0002-2500-7968

**Abhijit Bera** − *Department of Chemical and Biological Engineering, Iowa State University, Ames, Iowa 50011, United States*

**Rick W. Dorn** − *Department of Chemistry, Iowa State University, Ames, Iowa 50011, United States; U.S. Department of Energy, Ames Laboratory, Ames, Iowa 50011, United States*

**Yuqi Guo** − *Materials Science and Engineering, School for Engineering of Matter, Transport and Energy, Arizona State University, Tempe, Arizona 85287, United States*

**Qing Hua Wang** − *Materials Science and Engineering, School for Engineering of Matter, Transport and Energy, Arizona State University, Tempe, Arizona 85287, United States*

**Aaron J. Rossini** − *Department of Chemistry, Iowa State University, Ames, Iowa 50011, United States; U.S. Department of Energy, Ames Laboratory, Ames, Iowa 50011, United States;* orcid.org/0000-0002-1679-9203

**Julia V. Zaikina** − *Department of Chemistry, Iowa State University, Ames, Iowa 50011, United States;* orcid.org/0000-0002-8755-1926

**Luke T. Roling** − *Department of Chemical and Biological Engineering, Iowa State University, Ames, Iowa 50011, United States;* orcid.org/0000-0001-9742-2573

Complete contact information is available at: https://pubs.acs.org/10.1021/acsanm.3c00001


### Notes

The authors declare no competing financial interest.

## ACKNOWLEDGMENTS

This material is based upon work supported by the Air Force Office of Scientific Research under Award FA9550-20-10018. M.G.P. also acknowledges funding from the National Science Foundation Faculty Early CAREER Development Program (Grant DMR-1847370), which supported synchrotron-based X-ray scattering experiments. J.V.Z. acknowledges financial support from the National Science Foundation (Grant DMR-1944551) CAREER award. Q.H.W. and Y.G. acknowledge support from NSF Grant DMR-1906030. Use of the Advanced Photon Source at Argonne National Laboratory was supported by the U.S. Department of Energy, Office of Science, Office of Basic Energy Sciences, under Contract DEAC02-06CH11357. All PDF measurements were obtained through the rapid access

mail-in program. The authors thank Leighanne Gallington (Argonne National Laboratory) for collecting the total X-ray scattering data that were used for pair distribution function analysis. B.J.R. acknowledges support from the National Science Foundation Graduate Research Fellowship Program under Grant DGE-1744592. Solid-state NMR spectroscopy (R.W.D. and A.J.R) was supported by the U.S. Department of Energy (DOE), Office of Science, Basic Energy Science, Materials Science, and Engineering Division. The Ames Laboratory is operated for the U.S. DOE by Iowa State University under Contract DE-AC02-07CH11358. M.G.P. acknowledges support from the Herbert L. Stiles Faculty Fellowship from the Iowa State University College of Engineering. A.J.R. acknowledges additional support from the Alfred P. Sloan Foundation through a Sloan research fellowship. Any opinions, findings, conclusions, or recommendations expressed in this material are those of the authors and do not necessarily reflect the views of the National Science Foundation.

## REFERENCES

(1) Yamanaka, S.; Matsu-ura, H.; Ishikawa, M. New Deintercalation Reaction of Calcium from Calcium Disilicide. Synthesis of Layered Polysilane. *Mater. Res. Bull.* **1996**, *31* (3), 307−316.
(2) Molassioti-Dohms, A.; Dettlaff-Weglikowska, U.; Finkbeiner, S.; Hönle, W.; Weber, J. Photo- and Chemiluminescence from Wöhler Siloxenes. *J. Electrochem. Soc.* **1996**, *143* (8), 2674−2677.
(3) Dettlaff-Weglikowska, U.; Hönle, W.; Molassioti-Dohms, A.; Finkbeiner, S.; Weber, J. Structure and Optical Properties of the Planar Silicon Compounds Polysilane and Wöhler Siloxene. *Phys. Rev. B* **1997**, *56* (20), 13132−13140.
(4) Stutzmann, M.; Brandt, M. S.; Rosenbauer, M.; Weber, J.; Fuchs, H. D. Photoluminescence Excitation Spectroscopy of Porous Silicon and Siloxene. *Phys. Rev. B* **1993**, *47* (8), 4806−4809.
(5) Stutzmann, M.; Brandt, M. S.; Rosenbauer, M.; Fuchs, H. D.; Finkbeiner, S.; Weber, J.; Deak, P. Luminescence and Optical Properties of Siloxene. *J. Lumin.* **1993**, *57* (1), 321−330.
(6) Ryan, B. J.; Diroll, B. T.; Guo, Y.; Dolgos, C. J.; Wang, Q. H.; Roling, L. T.; Panthani, M. G. Silicon Nanosheets as Candidates for Silicon-Based Optoelectronics. *ECS Trans.* **2021**, *102* (1), 3.
(7) Zhang, F.-B.; Lv, S.-F.; Jiang, J.-X.; Ni, Y. Preparation of Siloxene Nanosheet-Supported Palladium as Sustainable Catalyst for Mizoroki−Heck Reaction. *Appl. Organomet. Chem.* **2014**, *28* (11), 826−830.
(8) Qian, C.; Sun, W.; Hung, D. L. H.; Qiu, C.; Makaremi, M.; Hari Kumar, S. G.; Wan, L.; Ghoussoub, M.; Wood, T. E.; Xia, M.; Tountas, A. A.; Li, Y. F.; Wang, L.; Dong, Y.; Gourevich, I.; Singh, C. V.; Ozin, G. A. Catalytic $CO_2$ Reduction by Palladium-Decorated Silicon−Hydride Nanosheets. *Nat. Catal.* **2019**, *2* (1), 46−54.
(9) Yan, X.; Sun, W.; Fan, L.; Duchesne, P. N.; Wang, W.; Kübel, C.; Wang, D.; Kumar, S. G. H.; Li, Y. F.; Tavasoli, A.; Wood, T. E.; Hung, D. L. H.; Wan, L.; Wang, L.; Song, R.; Guo, J.; Gourevich, I.; Jelle, A. A.; Lu, J.; Li, R.; Hatton, B. D.; Ozin, G. A. Nickel@Siloxene Catalytic Nanosheets for High-Performance $CO_2$ Methanation. *Nat. Commun.* **2019**, *10* (1), 2608.
(10) Kumai, Y.; Nakano, H. Characteristics of Layered Polysilane and Its Application to Lithium Ion Battery Anodes. *Jpn. J. Appl. Phys.* **2015**, *54* (3), 035201.
(11) Imagawa, H.; Itahara, H. Stabilized Lithium-Ion Battery Anode Performance by Calcium-Bridging of Two Dimensional Siloxene Layers. *Dalton Trans.* **2017**, *46* (11), 3655−3660.
(12) Liu, J.; Yang, Y.; Lyu, P.; Nachtigall, P.; Xu, Y. Few-Layer Silicene Nanosheets with Superior Lithium-Storage Properties. *Adv. Mater.* **2018**, *30* (26), 1800838.
(13) Krishnamoorthy, K.; Pazhamalai, P.; Kim, S.-J. Two-Dimensional Siloxene Nanosheets: Novel High-Performance Supercapacitor Electrode Materials. *Energy Environ. Sci.* **2018**, *11* (6), 1595−1602.
(14) An, Y.; Tian, Y.; Wei, C.; Jiang, H.; Xi, B.; Xiong, S.; Feng, J.; Qian, Y. Scalable and Physical Synthesis of 2D Silicon from Bulk Layered Alloy for Lithium-Ion Batteries and Lithium Metal Batteries. *ACS Nano* **2019**, *13* (12), 13690−13701.
(15) An, Y.; Tian, Y.; Wei, C.; Zhang, Y.; Xiong, S.; Feng, J.; Qian, Y. Recent Advances and Perspectives of 2D Silicon: Synthesis and Application for Energy Storage and Conversion. *Energy Storage Mater.* **2020**, *32*, 115−150.
(16) Brus, L. Luminescence of Silicon Materials: Chains, Sheets, Nanocrystals, Nanowires, Microcrystals, and Porous Silicon. *J. Phys. Chem.* **1994**, *98* (14), 3575−3581.
(17) Soref, R.; Buca, D.; Yu, S.-Q. Group IV Photonics: Driving Integrated Optoelectronics. *Opt. Photonics News* **2016**, *27* (1), 32−39.
(18) Little, B. E.; Chu, S. T. Toward Very Large-Scale Integrated Photonics. *Opt. Photonics News* **2000**, *11* (11), 24.
(19) Huey, W. L. B.; Goldberger, J. E. Covalent Functionalization of Two-Dimensional Group 14 Graphane Analogues. *Chem. Soc. Rev.* **2018**, *47* (16), 6201−6223.
(20) Karar, D.; Bandyopadhyay, N. R.; Pramanick, A. K.; Acharyya, D.; Conibeer, G.; Banerjee, N.; Kusmartseva, O. E.; Ray, M. Quasi-Two-Dimensional Luminescent Silicon Nanosheets. *J. Phys. Chem. C* **2018**, *122*, 18912.
(21) Ryan, B. J.; Hanrahan, M. P.; Wang, Y.; Ramesh, U.; Nyamekye, C. K. A.; Nelson, R. D.; Liu, Z.; Huang, C.; Whitehead, B.; Wang, J.; Roling, L. T.; Smith, E. A.; Rossini, A. J.; Panthani, M. G. Silicene, Siloxene, or Silicane? Revealing the Structure and Optical Properties of Silicon Nanosheets Derived from Calcium Disilicide. *Chem. Mater.* **2020**, *32* (2), 795−804.
(22) Akerkar, D. D.; Vaish, A. K.; Dhanjal, S. S.; Rao, G. N. *Calcium Silicide—Methods of Production and Their Technological Consideration*; NML: Jamshedpur, 1983; pp 180−186.
(23) Anderson, P. E.; Yee, K.; Homentowski, E.; Cheng, G.; Mehta, N.; Chen, G.; Stec, D., III; Hash, M. C.; Pearson, T.; Culter, R. A. Effect of Chemistry and Particle Size on the Performance of Calcium Disilicide Primers. Part 1-Synthesis of Calcium Silicide ($CaSi_2$) by Rotary Atomization. Army Armament Research Development and Engineering Center, Picatinny Arsenal NJ, Energetics Warheads and Manufacturing Technology Directorate, 2010.
(24) Fu, R.; Zhang, K.; Zaccaria, R. P.; Huang, H.; Xia, Y.; Liu, Z. Two-Dimensional Silicon Suboxides Nanostructures with Si Nanodomains Confined in Amorphous $SiO_2$ Derived from Siloxene as High Performance Anode for Li-Ion Batteries. *Nano Energy* **2017**, *39*, 546−553.
(25) Toby, B. H.; Von Dreele, R. B. GSAS-II: The Genesis of a Modern Open-Source All Purpose Crystallography Software Package. *J. Appl. Crystallogr.* **2013**, *46* (2), 544−549.
(26) Qiu, X.; Thompson, J. W.; Billinge, S. J. L. PDFgetX2: A GUI-Driven Program to Obtain the Pair Distribution Function from X-Ray Powder Diffraction Data. *J. Appl. Crystallogr.* **2004**, *37* (4), 678−678.
(27) Farrow, C. L.; Juhas, P.; Liu, J. W.; Bryndin, D.; Božin, E. S.; Bloch, J.; Proffen, T.; Billinge, S. J. L. PDFfit2 and PDFgui: Computer Programs for Studying Nanostructure in Crystals. *J. Phys.: Condens. Matter* **2007**, *19* (33), 335219.
(28) Harris, R. K.; Becker, E. D.; Cabral de Menezes, S. M.; Goodfellow, R.; Granger, P. NMR Nomenclature. Nuclear Spin Properties and Conventions for Chemical Shifts (IUPAC Recommendations 2001). *Pure Appl. Chem.* **2001**, *73*, 1795−1818.
(29) Sakellariou, D.; Lesage, A.; Hodgkinson, P.; Emsley, L. Homonuclear Dipolar Decoupling in Solid-State NMR Using Continuous Phase Modulation. *Chem. Phys. Lett.* **2000**, *319* (3), 253−260.
(30) Meiboom, S.; Gill, D. Modified Spin-Echo Method for Measuring Nuclear Relaxation Times. *Rev. Sci. Instrum.* **1958**, *29* (8), 688−691.
(31) Fung, B. M.; Khitrin, A. K.; Ermolaev, K. An Improved Broadband Decoupling Sequence for Liquid Crystals and Solids. *J. Magn. Reson.* **2000**, *142* (1), 97−101.
(32) Kubelka, P.; Munk, F. Ein Beitrag Zur Optik Der Farbanstriche. *Z. Tech. Phys.* **1931**, *12*, 593−601.


https://doi.org/10.1021/acsanm.3c00001
ACS Appl. Nano Mater. 2023, 6, 10054−10063

(33) Kresse, G.; Furthmüller, J. Efficient Iterative Schemes for Ab Initio Total-Energy Calculations Using a Plane-Wave Basis Set. *Phys. Rev. B* **1996**, *54* (16), 11169−11186.
(34) Kresse, G.; Furthmüller, J. Efficiency of Ab-Initio Total Energy Calculations for Metals and Semiconductors Using a Plane-Wave Basis Set. *Comput. Mater. Sci.* **1996**, *6* (1), 15−50.
(35) Perdew, J. P.; Burke, K.; Ernzerhof, M. Generalized Gradient Approximation Made Simple. *Phys. Rev. Lett.* **1996**, *77* (18), 3865−3868.
(36) Kresse, G.; Joubert, D. From Ultrasoft Pseudopotentials to the Projector Augmented-Wave Method. *Phys. Rev. B* **1999**, *59* (3), 1758−1775.
(37) Blöchl, P. E. Projector Augmented-Wave Method. *Phys. Rev. B* **1994**, *50* (24), 17953−17979.
(38) Monkhorst, H. J.; Pack, J. D. Special Points for Brillouin-Zone Integrations. *Phys. Rev. B* **1976**, *13* (12), 5188−5192.
(39) Nakano, H.; Nakano, M.; Nakanishi, K.; Tanaka, D.; Sugiyama, Y.; Ikuno, T.; Okamoto, H.; Ohta, T. Preparation of Alkyl-Modified Silicon Nanosheets by Hydrosilylation of Layered Polysilane ($Si_6H_6$). *J. Am. Chem. Soc.* **2012**, *134* (12), 5452−5455.
(40) Manfrinetti, P.; Fornasini, M. L.; Palenzona, A. The Phase Diagram of the Ca−Si System. *Intermetallics* **2000**, *8* (3), 223−228.
(41) Helbich, T.; Lyuleeva, A.; Höhlein, I. M. D.; Marx, P.; Scherf, L. M.; Kehrle, J.; Fässler, T. F.; Lugli, P.; Rieger, B. Radical-Induced Hydrosilylation Reactions for the Functionalization of Two-Dimensional Hydride Terminated Silicon Nanosheets. *Chem.—Eur. J.* **2016**, *22* (18), 6194−6198.
(42) Wöhler, L.; Müller, F. Uber die Calciumsilicide. *Z. Für Anorg. Allg. Chem.* **1921**, *120* (1), 49−70.
(43) Yaokawa, R.; Nakano, H.; Ohashi, M. Growth of $CaSi_2$ Single-Phase Polycrystalline Ingots Using the Phase Relationship between $CaSi_2$ and Associated Phases. *Acta Mater.* **2014**, *81*, 41−49.
(44) Gröbner, J.; Chumak, I.; Schmid-Fetzer, R. Experimental Study of Ternary Ca−Mg−Si Phase Equilibria and Thermodynamic Assessment of Ca−Si and Ca−Mg−Si Systems. *Intermetallics* **2003**, *11* (10), 1065−1074.
(45) Ma, X.; Xu, F.; Atkins, T. M.; Goforth, A. M.; Neiner, D.; Navrotsky, A.; Kauzlarich, S. M. A Versatile Low Temperature Synthetic Route to Zintl Phase Precursors: $Na_4Si_4$, $Na_4Ge_4$ and $K_4Ge_4$ as Examples. *Dalton Trans.* **2009**, No. 46, 10250−10255.
(46) Tu, C.; Ma, X.; Pantazis, P.; Kauzlarich, S. M.; Louie, A. Y. Paramagnetic, Silicon Quantum Dots for Magnetic Resonance and Two-Photon Imaging of Macrophages. *J. Am. Chem. Soc.* **2010**, *132* (6), 2016−2023.
(47) Atkins, T. M.; Thibert, A.; Larsen, D. S.; Dey, S.; Browning, N. D.; Kauzlarich, S. M. Femtosecond Ligand/Core Dynamics of Microwave-Assisted Synthesized Silicon Quantum Dots in Aqueous Solution. *J. Am. Chem. Soc.* **2011**, *133* (51), 20664−20667.
(48) Singh, M. P.; Atkins, T. M.; Muthuswamy, E.; Kamali, S.; Tu, C.; Louie, A. Y.; Kauzlarich, S. M. Development of Iron-Doped Silicon Nanoparticles As Bimodal Imaging Agents. *ACS Nano* **2012**, *6* (6), 5596−5604.
(49) Atkins, T. M.; Walton, J. H.; Singh, M. P.; Ganguly, S.; Janka, O.; Louie, A. Y.; Kauzlarich, S. M. EPR and Structural Characterization of Water-Soluble $Mn^{2+}$-Doped Si Nanoparticles. *J. Phys. Chem. C* **2017**, *121* (3), 1948−1956.
(50) Atkins, T. M.; Louie, A. Y.; Kauzlarich, S. M. An Efficient Microwave-Assisted Synthesis Method for the Production of Water Soluble Amine-Terminated Si Nanoparticles. *Nanotechnology* **2012**, *23* (29), 294006.
(51) Ma, X.; Wu, F.; Kauzlarich, S. M. Alkyl-Terminated Crystalline Ge Nanoparticles Prepared from NaGe: Synthesis, Functionalization and Optical Properties. *J. Solid State Chem.* **2008**, *181* (7), 1628−1633.
(52) Beekman, M.; Kauzlarich, S. M.; Doherty, L.; Nolas, G. S. Zintl Phases as Reactive Precursors for Synthesis of Novel Silicon and Germanium-Based Materials. *Materials* **2019**, *12* (7), 1139.
(53) Castillo, S. M.; Tang, Z.; Litvinchuk, A. P.; Guloy, A. M. Lattice Dynamics of the Rhombohedral Polymorphs of $CaSi_2$. *Inorg. Chem.* **2016**, *55* (20), 10203−10207.
(54) Nedumkandathil, R.; Benson, D. E.; Grins, J.; Spektor, K.; Häussermann, U. The 3R Polymorph of $CaSi_2$. *J. Solid State Chem.* **2015**, *222*, 18−24.
(55) Holder, C. F.; Schaak, R. E. Tutorial on Powder X-Ray Diffraction for Characterizing Nanoscale Materials. *ACS Nano* **2019**, *13* (7), 7359−7365.
(56) Deng, X.; Zheng, X.; Yuan, T.; Sui, W.; Xie, Y.; Voznyy, O.; Wang, Y.; Yang, Z. Ligand Impact of Silicanes as Anode Materials for Lithium-Ion Batteries. *Chem. Mater.* **2021**, *33* (23), 9357−9365.
(57) Dorn, R. W.; Ryan, B. J.; Lamahewage, S.; Dodson, M.; Essner, J. B.; Biswas, R.; Panthani, M. G.; Rossini, A. J. Chlorination of Hydrogenated Silicon Nanosheets Revealed by 1H{35Cl} and 29Si{35Cl} Solid-State NMR Spectroscopy. *Chem. Mater* **2023**, *35* (2), 539−548.
(58) Ryan, B. J.; Roling, L. T.; Panthani, M. G. Anisotropic Disorder and Thermal Stability of Silicane. *ACS Nano* **2021**, *15* (9), 14557−14569.
(59) Harris, J. T.; Hueso, J. L.; Korgel, B. A. Hydrogenated Amorphous Silicon (a-Si:H) Colloids. *Chem. Mater.* **2010**, *22* (23), 6378−6383.
(60) Sun, W.; Qian, C.; Cui, X. S.; Wang, L.; Wei, M.; Casillas, G.; Helmy, A. S.; Ozin, G. A. Silicon Monoxide − a Convenient Precursor for Large Scale Synthesis of near Infrared Emitting Monodisperse Silicon Nanocrystals. *Nanoscale* **2016**, *8* (6), 3678−3684.
(61) Hanrahan, M. P.; Fought, E. L.; Windus, T. L.; Wheeler, L. M.; Anderson, N. C.; Neale, N. R.; Rossini, A. J. Characterization of Silicon Nanocrystal Surfaces by Multidimensional Solid-State NMR Spectroscopy. *Chem. Mater.* **2017**, *29* (24), 10339−10351.
(62) Dorn, R. W.; Marro, E. A.; Hanrahan, M. P.; Klausen, R. S.; Rossini, A. J. Investigating the Microstructure of Poly(Cyclosilane) by $^{29}$Si Solid-State NMR Spectroscopy and DFT Calculations. *Chem. Mater.* **2019**, *31* (21), 9168−9178.
(63) Trout, A. H.; Wang, Y.; Esser, B. D.; Jiang, S.; Goldberger, J. E.; Windl, W.; McComb, D. W. Identification of Turbostratic Twisting in Germanane. *J. Mater. Chem. C* **2019**, *7* (32), 10092−10097.
(64) Welberry, T. R. Hexagonal Paracrystals. *Z. Für Krist. - Cryst. Mater.* **2015**, *230* (1), 69−74.
(65) Haas, P.; Tran, F.; Blaha, P. Calculation of the Lattice Constant of Solids with Semilocal Functionals. *Phys. Rev. B* **2009**, *79* (8), 085104.
(66) Delerue, C.; Allan, G.; Reynaud, C.; Guillois, O.; Ledoux, G.; Huisken, F. Multiexponential Photoluminescence Decay in Indirect-Gap Semiconductor Nanocrystals. *Phys. Rev. B* **2006**, *73* (23), 235318.
(67) Finkbeiner, S.; Weber, J.; Rosenbauer, M.; Stutzmann, M. Transient Photoluminescence Decay in Porous Silicon and Siloxene. *J. Lumin.* **1993**, *57* (1), 231−234.
(68) Pavesi, L.; Ceschini, M. Stretched-Exponential Decay of the Luminescence in Porous Silicon. *Phys. Rev. B* **1993**, *48* (23), 17625−17628.


https://doi.org/10.1021/acsanm.3c00001
*ACS Appl. Nano Mater.* 2023, 6, 10054−10063